Available online at www.sciencedirect.com
SCIENCE DIRECT
Remote Sensing of Environment 85 (2003) 339–354
Remote Sensing of Environment
www.elsevier.com/locate/rse

Canopy attributes of desert grassland and transition communities derived from multiangular airborne imagery

Mark J. Chopping[a,*], Albert Rango[a], Kris M. Havstad[a], Frank R. Schiebe[b], Jerry C. Ritchie[c], Thomas J. Schmugge[c], Andrew N. French[c], Lihong Su[d], Lynn McKee[c], M. Rene Davis[e]

[a] *USDA-ARS Jornada Experimental Range, 2995 Knox St., Las Cruces, NM 88003, USA*
[b] *SST Development Group, Inc., Stillwater, OK 74701, USA*
[c] *USDA-ARS Hydrology and Remote Sensing Laboratory, BARC-W, Beltsville, MD 20705, USA*
[d] *Research Center for Remote Sensing, Beijing Normal University, Beijing 100875, PR China*
[e] *USDA-ARS Subtropical ARS, Integrated Farming and Natural Resources Research Unit, Weslaco, TX 78596, USA*

Received 1 April 2002; received in revised form 6 December 2002; accepted 15 December 2002

Abstract

The surface bidirectional reflectance distribution function (BRDF) contains valuable information on canopy physiognomy for desert grassland and grass–shrub transition communities. This information may be accessed by inverting a BRDF model against sets of observations, which encompass important variations in viewing and illumination angles. This paper shows that structural canopy attributes can be derived through inversion of the Simple Geometric Model (SGM) of the BRDF developed in this paper. It is difficult to sample BRDF features from the ground because of the discontinuous nature of the canopies and long intrinsic length scales in remotely sensed spectral measures (>10 m). A multispectral digital camera was therefore used to derive spatial multiangular reflectance data sets from the air and the SGM was validated against and inverted with these. It was also validated using 3-D radiosity simulations driven with maps of field-measured plant dimensions. The interpretation of the retrieved parameter maps (shrub density, shrub width and canopy height) reveals variations in canopy structure within desert grassland and grassland–shrubland transition communities, which are clearly related to structural and optical features in high resolution panchromatic and vegetation index images. To our knowledge, this paper reports on the first attempts to acquire structural canopy attributes of desert landscapes using multiple view angle data at scales less than 1 km. The results point to further opportunities to exploit multiangular data from spaceborne sensors such as the Multiangle Imaging SpectroRadiometer (MISR) and the Compact High Resolution Imaging Spectrometer (CHRIS) on the NASA Terra and European Space Agency's PROBA satellites, respectively.

Keywords: Desert grassland; Transition communities; Multiangular airborne imagery

1. Introduction

The surface bidirectional reflectance distribution function (BRDF) is dependent on and contains information on the structure and optical properties of surface elements, some of which may be determined by adjustment of a model against sets of multiangular spectral reflectance observations (Privette et al., 2000; Qi, Huete, Cabot, & Chehbouni, 1994). BRDF models are formulated to predict BRDF for surfaces described by parameters such as leaf area index, leaf angle distribution, canopy gap size, plant dimensions (height and diameter), proportional planimetric cover and soil albedo, among others, and may thus provide some or all of these on model inversion. However, no physical models are able to accommodate the complex canopies presented by southwestern US desert grasslands and shrublands and inversions can easily be compromised by model complexity and large numbers of parameters. On the other hand, semi-empirical models such as linear, semi-empirical, kernel-driven (LiSK) models are able to encapsulate directional signals which are potentially very useful in detailed land cover classification and community type mapping over large areas (Chopping, 2000; Chopping, Rango, & Ritchie, 2002) but have few or no parameters with a direct physical interpretation. An ideal model might provide some physical parameters on inversion

* Corresponding author. Current address: Earth and Environmental Studies, Montclair State University, Upper Montclair, NJ 07043, USA. Tel.: +1-973-655-7384; fax: +1-973-655-4072.
E-mail address: chopping@pegasus.montclair.edu (M.J. Chopping).

0034-4257/03/$ - see front matter © 2003 Elsevier Science Inc. All right reserved.
doi:10.1016/S0034-4257(03)00012-9

while remaining viable with respect to inversion with a data set providing a limited angular coverage. Work towards such a model, the Simple Geometric Model (SGM), is presented here. The SGM was validated using both 3-D modeling with the Radiosity Graphics Method (RGM; Qin & Gerstl, 2000) driven by detailed plant maps, and using multiangle observations from the air. It was then tested for the ability to retrieve physical canopy attributes over desert grassland and grass–shrub transition communities using these data.

There are two main requirements for properly sampling the BRDF: multiple looks at a wide range of viewing and solar angles, preferably including the principal plane (PP); and a ground-projected instantaneous field-of-view (GIFOV) large enough to encompass a representative sample of surface elements. The surface intrinsic length scale may be one or two orders of magnitude greater than the width of the largest commonplace vegetation or other spatial element (i.e. shrub, grass or soil patch) placing physical constraints on footprint size: a sensor with a GIFOV of 0.2 m will not capture the BRDF of the surface but of surface components (e.g. parts of shrubs). The first requirement is not met by any spaceborne sensor and the second is difficult to meet with ground-based radiometers or spectrometers unless the assumption of an homogeneous surface is made. This assumption is likely to be poor for the discontinuous canopies of desert plant communities. Until the mid-1990s, only a few remote sensing studies considering surface BRDF had been carried out over desert grassland and shrubland sites on the JER. The earlier studies were concerned with the relationships between spectral reflectance or spectral vegetation indices and community composition (Duncan, Stow, Franklin, & Hope, 1993; Franklin, Duncan, & Turner, 1993; Franklin & Turner, 1992). The earliest of these evaluated the application of a geometric-optical canopy reflectance model to semiarid shrub vegetation; however, the model was inverted with single view angle multispectral data from the SPOT HRV XS sensor so the geometric-optical model is effectively reduced to a spectral mixture model. More recently, a number of point or spatially averaged BRDF data sets were acquired at a grassland–shrubland transition site as part of the 1997 Grassland Prototype Validation Exercise (PROVE) experiment, including spectral reflectance factor measurements from towers, from the air and from just above the ground (Privette et al., 2000).

In this study, several targets were chosen to represent a range of vegetation conditions spanning desert grasslands and grass–shrub transitional zones. These target areas were located in the USDA-ARS Jornada Experimental Range (JER), 37 km NE of Las Cruces, NM. The two communities do not differ greatly in terms of aboveground biomass (gC/m^2) and primary production (Huenneke, Anderson, Schlesinger, & Remmenga, 2001) but do differ importantly with respect to species composition, canopy physiognomy and lacunarity. This is an important location not only because it is a NASA Earth Observing System (EOS) Core Site but also because many other remote sensing, biophysical, and ecological data sets are being collected here (Havstad, Kustas, Rango, Ritchie, & Schmugge, 2000). For example, the USDA-ARS Hydrology and Remote Sensing Laboratory's JORNada EXperiment (JORNEX) series has been ongoing since 1995 (Rango et al., 1996). Recently (2000), the JER was adopted by the European Space Agency as a Compact High Resolution Imaging Spectrometer (CHRIS)/PROBA Mission Core Test Site, with teams from Britain and the USA engaged to validate and exploit CHRIS data (BNSC, 2002; http://www.chris-proba.org.uk).

2. Methods

2.1. Multiangular reflectance data

The DuncanTech camera (Model: MS2100[1]) used to acquire the multiangular imagery was a three-charge-coupled device (CCD) progressive scan digital camera using a color-separating prism, trim filters and three sensors to provide multispectral images in three channels (500, 650 and 800 nm). Variable viewing zeniths were obtained by mounting the camera on a tilting bracket and adjusting the tilt along the flightline. The target area extents were 200 and 8 m^2 tarpaulins ("tarps") of 4% and 32% spectral reflectance (green–red wavelength, nadir, diffuse) were positioned on a flat surface at the grass site to aid in calibration of the imagery (Moran, Bryant, Clarke, & Qi, 2001). The flying altitude was 1800 to 2200 m above ground level resulting in a GIFOV of ~ 2 m^2. The flights took place at three times a day to sample at three different solar zenith angles and close to the PP (Fig. 1). All images were registered to a subset of a 1-m panchromatic IKONOS[1,2] scene. The output 2-m co-registered images are not immediately suitable for the purpose of accessing the BRDF because the GIFOV does not adequately sample all surface components contributing to it. Researchers have found that as long as the scale of the observation is larger than the intrinsic length scale of the surface, the BRDF can be adequately represented by a linear combination of the BRDFs of elements of that surface (Brown de Colstoun et al., 1996; Leroy, Bicheron, & Hautecoeur, 1997; Qin & Gerstl, 2000). Pelgrum, Schmugge, Rango, Ritchie, and Kustas (2000) sought intrinsic length scales of normalized difference vegetation index (NDVI), temperature and albedo over these sites using geostatistical methods and found that the minimum was around 8–11 m, implying that a minimum 8–11-m GIFOV would be required to provide a representative sample of the BRDF. The 2-m images were thus convolved with a 25×25-cell pseudo-Gaussian point spread function (PSF) in order to

[1] Trade names are included for the benefit of the reader and do not imply an endorsement of or a preference for the product listed by the U.S. Department of Agriculture.

[2] An advanced high-resolution multispectral spaceborne sensor operated by Space Imaging.

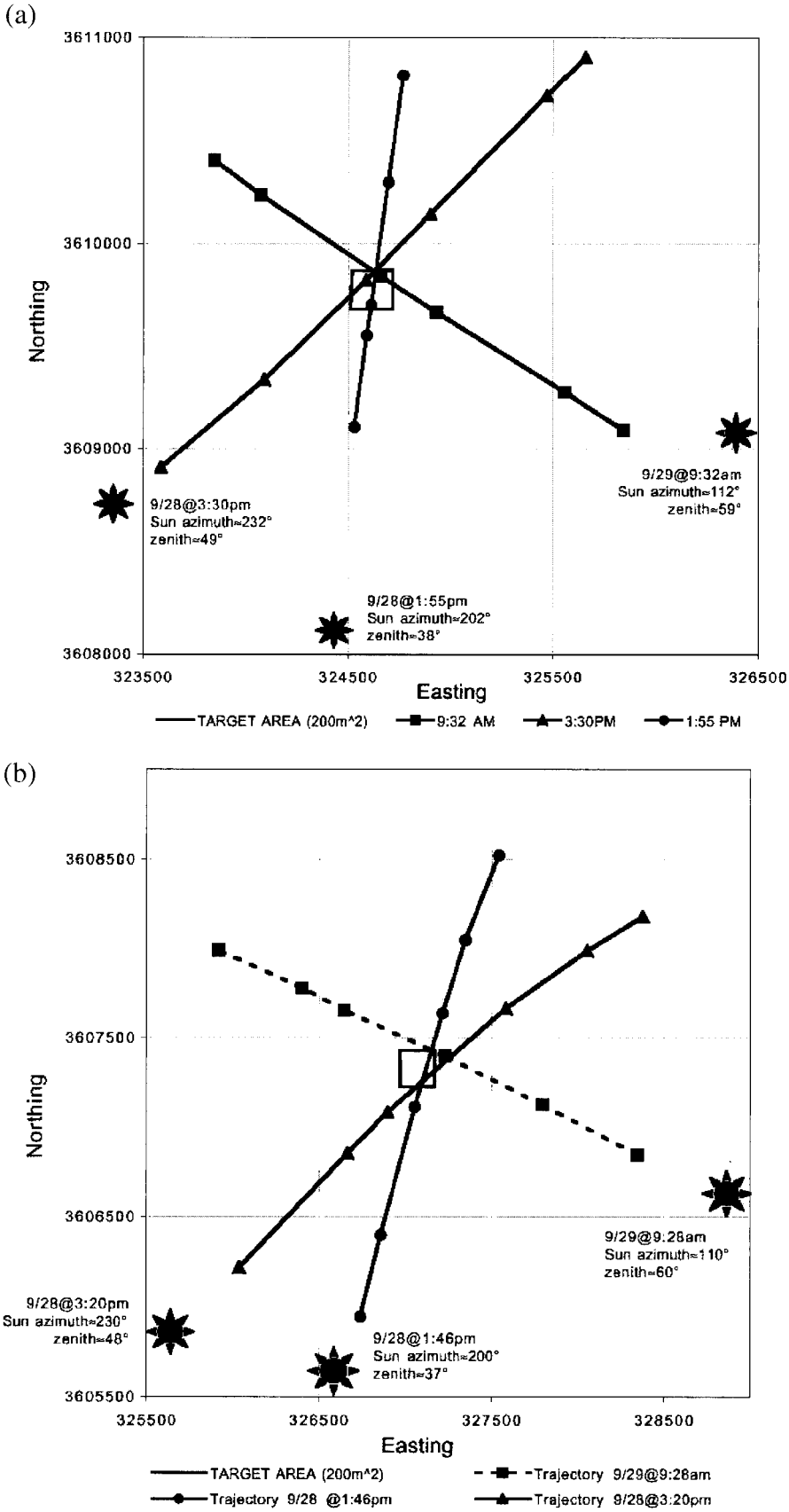

Fig. 1. Cessna 404 trajectories and DuncanTech camera image locations on a UTM grid (coordinates: meters) over (a) the transition site and (b) the grass site (UTM grid), at three times a day (three solar zenith and azimuth angles). Boxes are 200 m^2 target areas.

simulate a larger GIFOV sensor (Hlavka, 1986) and the convolved images were sampled at a 25-m interval. Grids of view zenith and azimuth angles were calculated using the aircraft Global Positioning System data and sun angles were calculated using the POSSOL routine of 6S (Vermote, Tanre, Deuze, Herman, & Morcrette, 1997).

Only the red (650 nm) channel data were used in subsequent model validation and inversion because in these wavelengths absorption by plant photosynthetic materials and pigments is maximal (and so contrast between soil and vegetation is maximal) and the single scattering approximation is more valid than in the near infra-red. Qin and Gerstl (2000) also point out that the linear mixture assumption underlying geometric-optical (GO) models is more valid for the red than near infra-red wavelengths. Recent BRDF model inversion experiments using numerical methods (Gemmell, 2000) show that there are generally fewer problems such as trapping at local minima (saddle points in the merit function surface) in the red compared to the near infra-red wavelengths. This is corroborated by recent work by Pinty, Widlowski, Gobron, Verstraete, and Diner (2002), which asserts that the wavelength should be chosen to maximize the reflectance/absorption contrast between vertically clumped elements and the background. Introducing spectral variation would add a further level of complexity while the intention here is to keep the modeling problem as simple as possible: if flawed results are obtained at a single, optimal wavelength, adding data in other, sub-optimal wavelengths is unlikely to be helpful.

Calibration of the digital numbers from the DuncanTech camera images to spectral radiance ($W/m^2/\mu m/sr$) was achieved through laboratory tests using an integrating sphere (Schiebe, Waits, Everitt, & Duncan, 2001) and checked by measuring against the spectral radiance of targets with known reflectance properties (Moran et al., 2001). Nominal 32% and 4% reference tarps were deployed on the ground and hemispherical–directional reflectance factors for the 32% tarp (marked Tracor GIE, Provo, UT, Dual Role Panel "RST-8625—32%" serial # 193972) were measured using a simple field goniometer fitted with a small four-band radiometer (1° IFOV). Measurements were made in the principal and cross-principal planes with view zenith angles ranging ± 50° at increments of 10°. Nadir spectra of both the 4% and 32% tarps were acquired with an ASD FieldSpec Pro[1] spectroradiometer concurrently with the angular radiance measurements (Fig. 2(a)). The code 6S version 4.2 (Vermote et al., 1997) was used to retrieve spectral–directional reflectance in the DuncanTech 650-nm channel at the surface, assuming a Lambertian surface, visibility of 50 km, a McClatchey midlatitude summer standard atmospheric model, and the Shettle model for background desert aerosol, with water vapor, aerosol and ozone content under the plane estimated. Near-nadir spectral radiance values from the DuncanTech acquired over the 32% and 4% tarps were checked against spectra averaged for the DuncanTech red channel ($n=41$). A good relation was found between nadir

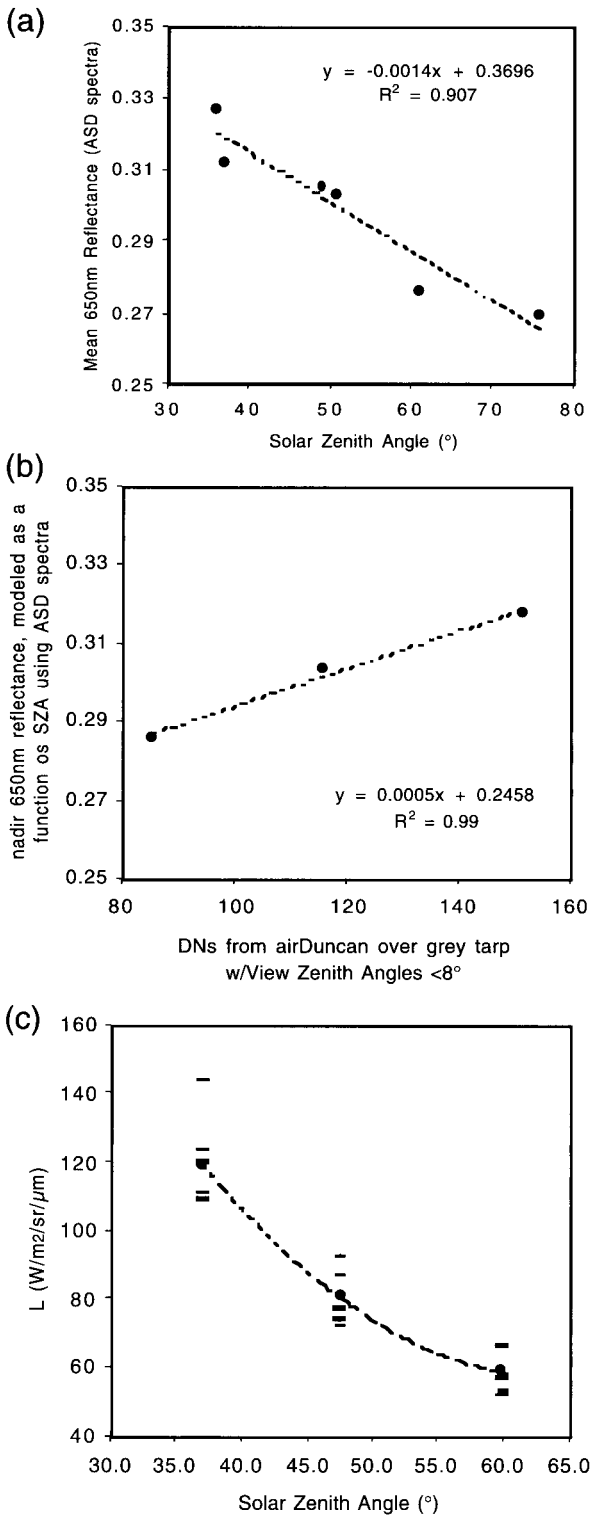

Fig. 2. (a) Relation between SZA and mean nadir 650 nm grey (32%) tarp spectral reflectance (average over 41 samples); (b) relation between DuncanTech DNs and 650-nm reflectance modeled as a function of SZA; (c) DuncanTech spectral radiance ($W/m^2/\mu m$) at 650 nm as a function of SZA: bars show the divergence owing to view zenith angle, dots are the means for each SZA, and the dotted line is a second-order polynomial fitted through the means.

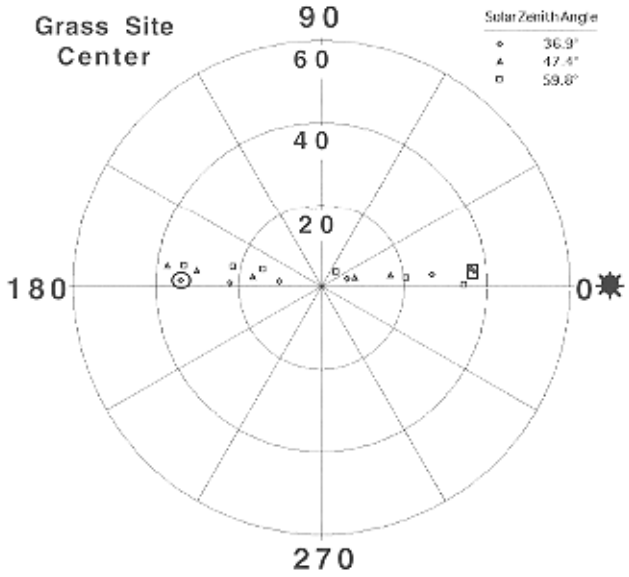

Fig. 3. Polar plot of the angular sampling achieved in the September 2000 campaign at the center of the grass site. The radial axis defines the azimuthal orientation with the sun located at 0°. The large square and circle indicate observations close to the hot spot and specular geometries, respectively.

tarp 650-nm reflectance factor and solar zenith angle (Fig. 2(b))—noting that $n=3$—and the variation of values with both solar and view zenith angles is important (Fig. 2(c)).

A typical angular sampling for one location is shown in Fig. 3. It can be seen that the observations all lie quite close to the PP with a very small offset. Since the images do not overlap, there are varying numbers of observations at different view angles (means are 9 and 14 for the grass and transition sites, respectively). Uncertainties (the difference between off-nadir and nadir reflectance values divided by the nadir reflectance value) owing to anisotropy are as high as 80%; a similar level to those found by Qi, Huete et al. (1994) over a semiarid grassland in Arizona. The range and configuration of the angular samples can be more important than the number of samples (Flasse, 1993) although many BRDF models are not formulated to replicate configurations such as the hot spot and specular regions and screening for these is required. The effects of the hot spot can be appreciated by comparing a 650-nm DuncanTech image over the grass target with an IKONOS panchromatic image chip of the same area acquired close to nadir and with a solar zenith of 23° (Fig. 4). Data acquired at these configurations were screened conservatively within a 5° domain.

2.2. Modeling the BRDF

Physical BRDF models are unable to accommodate the canopy–soil complexes of southwestern US desert grasslands and shrublands, so modelers have turned to hybrid

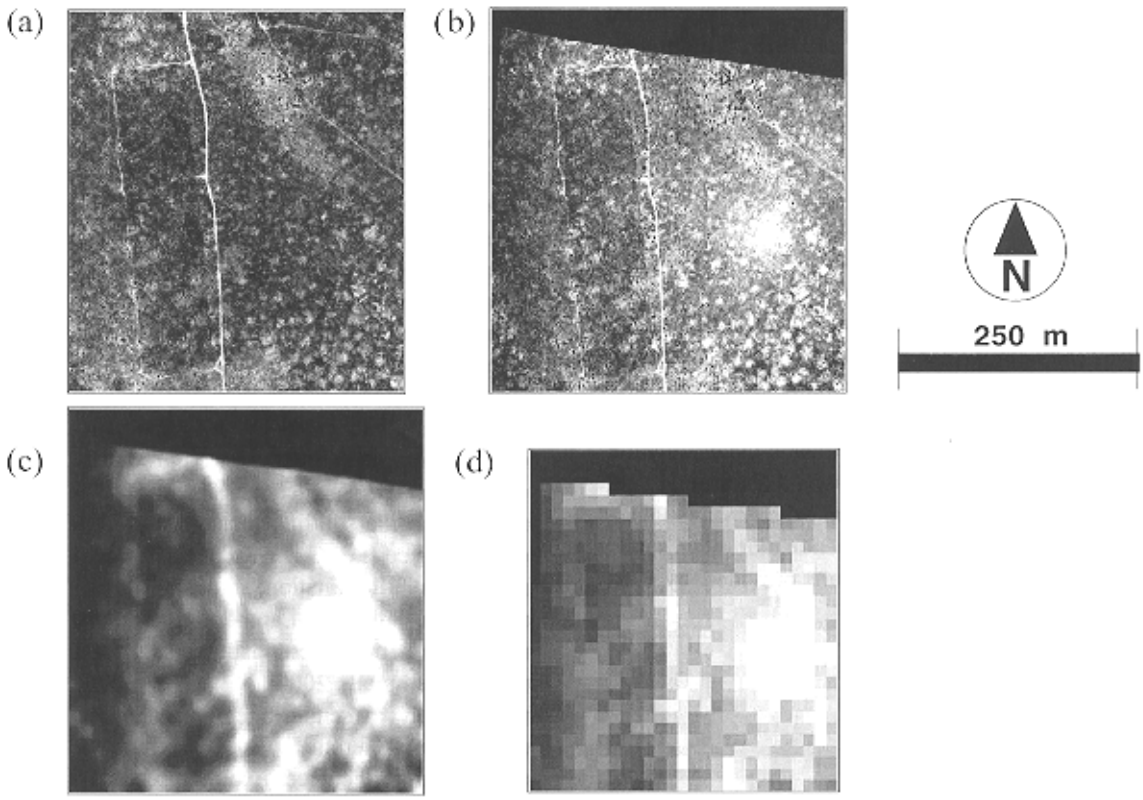

Fig. 4. (a) Panchromatic IKONOS image chip over the grass site, (b) DuncanTech 650 nm channel image resampled to 2 m (note hot spot area), (c) DuncanTech image convolved with a 50-m pseudo-Gaussian kernel to simulate a large IFOV sensor image, (d) the same image, nearest-neighbor sampled every 25 m.

geometric-optics/radiative transfer (GORT) formulations. These seek to combine the ability to describe the discrete nature of discontinuous canopies of the GO approach with the RT approach to volume scattering within crowns (Chen, Li, Nilson, & Strahler, 2000; Jupp et al., 1994; Li, Strahler, & Woodcock, 1995). Ni and Li (2000) present a detailed adaptation of the GORT concept for sparse, discontinuous shrubland canopies which has given good results when tested in forward mode against POLDER and AVHRR data sets. The main limitation of current GORT models is that invertibility may be compromised, partly as a result of a large number of adjustable parameters—it may be unwise to attempt to invert for more than three or four parameters (Barnsley, Allison, & Lewis, 1997)—and partly from inherent model complexity. An ideal model would have a small number of adjustable physical parameters while remaining capable of describing a wide range of surface anisotropies. It might fall somewhere between the more complex GORT and the simplified LiSK formulations and would retain the ability of both types to accommodate both large- (inter-plant) and small-scale (crown-level) volume scattering phenomena. The model should be further refined by also considering the BRDF of the soil or soil/litter background (Ni & Li, 2000).

2.3. SGM derivation

Taking the work of Wanner, Li, and Strahler (1995) as a starting point but accounting for the spectral directional reflectance or what some workers call the "component signatures" of the two most important scene elements: bare soil (G) and plant leaves (C), and assuming an optically thin medium, it is possible to arrive at the formulation in Eq. (1)

$$R = Gk_G(\vartheta_i,\ \vartheta_v, \varphi) + R_{thin}k_C(\vartheta_i,\ \vartheta_v, \varphi) \quad (1)$$

where R is modeled reflectance; G is the spectral signature of bare soil; $k_G(\vartheta_i, \vartheta_v, \varphi)$ and $k_C(\vartheta_i, \vartheta_v, \varphi)$ are the proportions of sunlit ground and shrub crown visible to a sensor at a particular geometry (ϑ_i = solar zenith, ϑ_v = view zenith and φ = relative azimuth); and R_{thin} is a volume scattering function (the Ross–Thin kernel of Wanner et al., 1995). The contribution of geometric effects is estimated via calculation of the proportions of sunlit and viewed background and crown (k_G and k_C). These are calculated exactly via Boolean geometry for the principal and perpendicular planes and approximated away from these and are provided by Eqs. (2) and (3), respectively.

$$k_G = e^{-\lambda\pi r^2\{\sec\vartheta_i'+\sec\vartheta_v'-O(\vartheta_i,\ \vartheta_v,\ \varphi)\}} \quad (2)$$

$$k_C = (1 - e^{-\lambda\pi r^2\sec\vartheta_v'})\frac{1}{2}(1+\cos\varepsilon') \quad (3)$$

where λ is the number density of objects; r is the average radius of these objects; ϑ_i, ϑ_v and φ are the solar zenith, view zenith, and relative azimuth angles, respectively; O is the overlap area between the shadows of illumination and viewing. These functions include the parameters b/r (vertical crown radius/horizontal crown radius) and h/b (height of crown center/vertical crown radius), which describe the shape and height of the crown. The prime indicates equivalent zenith angles obtained by a vertical scale transformation in order to treat spheroids as spheres ($\vartheta' = \tan^{-1}(b/r \tan \vartheta)$ see Wanner et al. (1995). In this study, b/r is fixed at 1.0 and h/b is fixed at 1.5 or optionally left as a free parameter. ε is the scattering phase angle given by Eq. (4)

$$\cos\varepsilon = \cos\vartheta_i\cos\vartheta_v + \sin\vartheta_i\sin\vartheta_v\cos\varphi \quad (4)$$

In the derivation of the Li kernels for the LiSK models in the Algorithm for Modeling [MODIS] Bidirectional Reflectance Anisotropies of the Land Surface (AMBRALS) suite, Wanner et al. (1995) take the sunlit crown and ground to be equally bright (i.e. $C = G$, respectively) but here the components were initially allocated signatures based on average values from field reflectance spectra and previous studies: green leaf reflectance at 650 nm is set at 0.09 and bare soil reflectance at 0.25 (Asner, Wessman, Bateson, & Privette, 2000; Everitt et al., 1997). The contribution from the soil/litter background is then estimated as the product of the bare soil signature and the fraction of illuminated and visible bare soil (Gk_G) and the spectral reflectance of green leaves enters into the calculation of the contribution from volume scattering, which is determined by the Ross–Thin approximation in Eq. (5)

$$R_{thin} = \frac{2\rho_L LAI}{3\pi}\frac{(\pi/2-\varepsilon)\cos\varepsilon + \sin\varepsilon}{\cos\vartheta_i + \cos\vartheta_v} + \rho_0 \quad (5)$$

where ε is the scattering phase angle (Eq. (4)). The rightmost term, ρ_0, is the average (assumed) Lambertian reflectance of the layer beneath the thin topmost part of the canopy, ρ_L is the (assumed) Lambertian reflectance of scattering facets—leaves, non-photosynthetic vegetation (litter and woody plant parts)—and LAI is the product of facet volume density and area measured for the full height of the canopy. Note that ρ_0 refers only to the background directly under crowns (shrub understory) rather than the total background since the remaining background is accounted for by the contribution from illuminated and viewed ground.

There are two inadequacies with this formulation as it stands. First, the soil/litter background is treated as a Lambertian surface (i.e. G is a fixed value and is invariant with viewing and illumination angles). The importance of accounting for the non-Lambertian property of the "background" has been demonstrated by a number of recent studies (Gemmell, 2000; Ni & Li, 2000) with a greater impact likely in semiarid environments where vegetation cover is low. Gemmell (2000) showed that variations in background reflectances would preclude the retrieval of forest structural characteristics at low to intermediate covers unless these variations can be taken into account in inversion. Second, the behavior of the volume scattering function with LAI is not as expected: when the green leaf density of

the protrusions increases, the magnitude of volume scattering also increases, counter to expectations. The first weakness is dealt with by injecting a soil (transition site) or soil–grass (grass site) background BRDF into the model by replacing the component signature G with a modeled value dependent on the viewing and illumination geometry. This is achieved empirically by adjusting the Walthall model (Walthall, Norman, Welles, Campbell, & Blad, 1985) against ground-based bidirectional reflectance factor (BRF) measurements over bare soil close to the transition site made by a group at the University of Nebraska-Lincoln (UNL) as part of NASA's 1997 Grassland PROVE campaign using a SE590 spectroradiometer. The root mean-square error (RMSE) of the model fitting was 0.018 with a R^2 of 0.63. The fitting was to a large data set consisting of 54 reflectance values split equally in the principal and perpendicular planes with view and solar zeniths in the ranges $\pm 60°$ and 33–56°, respectively (fitting to just the principal plane resulted in a similar RMSE but an R^2 of 0.78). A number of other models are capable of providing a soil BRDF as the lower boundary layer but the Walthall model performs well here in this capacity, as elsewhere (Kuusk & Nilson, 2000; Ni & Li, 2000). A similar background BRDF is provided for the grass site. In this case, there were 108 observations again split equally in the principal and perpendicular planes with view and solar zeniths in the ranges $\pm 60°$ and 28–61°, respectively, over the grass at two different locations with equally good model fitting (RMSE = 0.009; $R^2 = 0.85$).

The second weakness is dealt with by adopting the simplified Ross turbid medium approximation for optically thin or thick plane parallel canopies (Ross, 1981). Ross' formula was simplified by both Roujean, Leroy, Deschamps

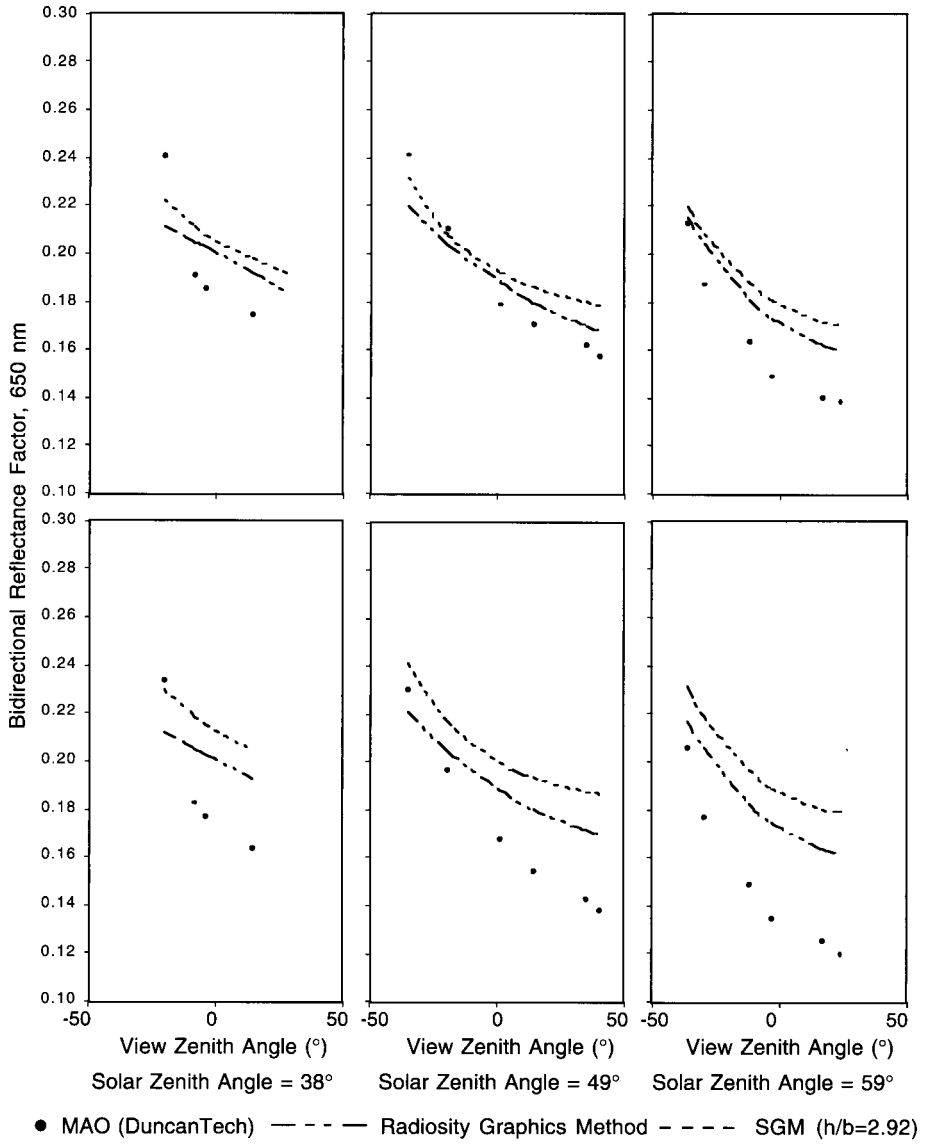

Fig. 5. SGM (with parameters mean plant density, radius and b/r ratio from field survey), RGM output and multiangle observations from the tilted, airborne DuncanTech MS2100 camera. Top row: Plot 107 (sparse snakeweed). Bottom row: Plot 108 (dense snakeweed). Modeling was for 25 m^2 plots.

Table 1
Canopy statistics from aerial photography and field survey and SGM validation

	Plot #107 (sparse)	Plot #108 (dense)
Mean plant radius (m)	0.230	0.168
Mean plant height (m)	0.337	0.234
Mean *b/r*	0.863	0.765
Plant density (#/m^2)	0.661	1.093
RMSE vs. observations	0.021	0.039
RSQ vs. observations	0.914	0.931
RMSE vs. RGM	0.008	0.015
RSQ vs. RGM	0.981	0.982

Plot #107: small number of large shrubs, few snakeweed, much bare soil; plot #108: dense snakeweed, fewer large shrubs, less bare soil; *b/r*: a ratio of crown vertical to horizontal dimensions (shape factor); observations: multiangular BRFs at 6 view × 3 solar zeniths angles; RGM: radiosity graphics method (Qin & Gerstl, 2000).

(1992) and Wanner et al. (1995) to obtain the following function as an initial step in the derivation of LiSK model kernels Eq. (6)

$$C_{\mathrm{Ross}} = \frac{4\rho_{\mathrm{L}}}{3\pi}\frac{(\pi/2-\varepsilon)\cos\varepsilon+\sin\varepsilon}{\cos\vartheta_{\mathrm{i}}+\cos\vartheta_{\mathrm{v}}}(1-\Delta)+\rho_0\Delta \quad (6)$$

where

$$\Delta = \mathrm{e}^{-[0.5\mathrm{LAI}(\sec\vartheta_{\mathrm{i}}+\sec\vartheta_{\mathrm{v}})]} \quad (7)$$

This function is incorporated into the model by assuming a rather lower average reflectance for the understory directly underneath shrub crowns ($\rho_0 = 0.05$) than for sunlit and viewed background, represented in the model by the calibrated Walthall BRDF model (range 0.23–0.29). The entire model formulation is then (Eq. (8))

$$R = G_{\mathrm{Walthall}}(\vartheta_{\mathrm{i}},\ \vartheta_{\mathrm{v}},\ \varphi)k_G(\vartheta_{\mathrm{i}},\ \vartheta_{\mathrm{v}},\ \varphi) + C_{\mathrm{Ross}}(\vartheta_{\mathrm{i}},\ \vartheta_{\mathrm{v}},\ \varphi)k_C(\vartheta_{\mathrm{i}},\ \vartheta_{\mathrm{v}},\ \varphi) \quad (8)$$

The SGM is highly simplified as it has been derived primarily with inversion in mind and as a result has a number of limitations: the linear combination of terms is somewhat empirical, and there is no term to account specifically for the diffuse component (it is assumed that the direct/diffuse ratio is rather high in the red wavelengths, so shadows are taken as absolutely black). Multiple scattering between plants is ignored although this is likely to make a small contribution in the red wavelengths.

2.4. SGM validation protocol

The SGM was tested against both the multiangular data set acquired from the air and against azimuthal BRDF slices simulated using the Radiosity Graphics Method (RGM) of Qin and Gerstl (2000). The RGM is a 3-D scene modeling package capable of using plant architectures modeled with L-systems codes together with radiosity techniques. Radiosity is based on scene geometry alone rather than on particular viewing/illumination sampling régimes: all energy emitted or reflected by every surface in a scene is accounted for by its reflection and absorption by other surfaces. The rate at which energy leaves a surface (the radiosity) is the sum of the rates at which the surface emits energy and reflects or transmits it from other surfaces. To calculate BRDF, all light interactions in an environment are calculated independent of view (Disney, 2002). The RGM was driven by maps of plant locations, types and dimensions for two 25 m^2 plots, obtained from combining aerial photography and meticulous field survey carried out along linear 1-m-wide quadrat series. The two plots were chosen to represent extremes in small plant density (mostly broom snakeweed), with optical properties of the different plant and soil components obtained from the

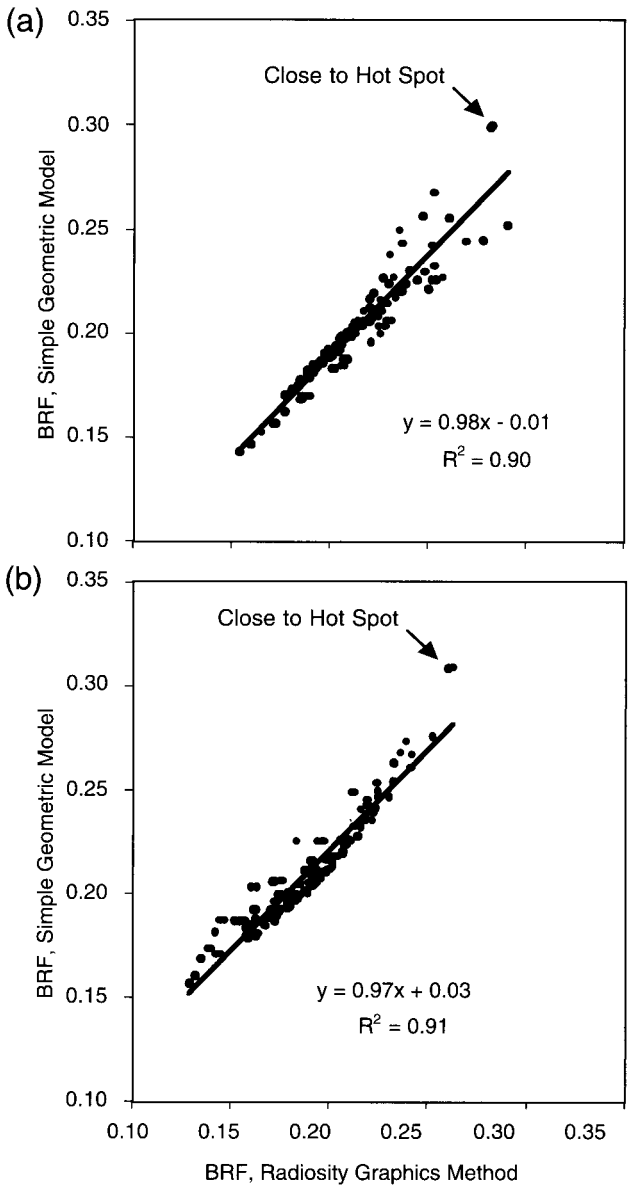

Fig. 6. Relationship between BRFs from the SGM and RGM for a wide range of viewing zenith and relative azimuth angles and at three sun angles, (a) sparse and (b) dense understory case.

literature (Asner et al., 2000; Everitt et al., 1997; White, Asner, Nemani, Privette, & Running, 2000).

2.5. SGM inversion protocol

Adjustment of the SGM against the sets of multiangular observations was effected by an adaptation of the Hooke and Jeeves (1961) direct search algorithm. The inversion criterion was the minimization of the absolute differences between the modeled and observed reflectance values; i.e. the mean-square-error term in Eq. (9)

$$\partial^2 = \frac{1}{n}\sum_{i=1}^{n}(\rho_{\mathrm{mod}_i} - \rho_{\mathrm{obs}_i})^2 \quad (9)$$

where ρ_{obs} is the observed reflectance, ρ_{mod} is modeled reflectance, n is the number of observations and i is the multiangular observation instance. The optimizations were effected with either two or three adjustable model parameters: λ, LAI and (optionally) r (the average radius of shrubs). Constraints were imposed on canopy height (≤ 4 m), canopy fractional cover (≤ 0.9) and LAI (≥ 0.0), with height and cover calculated from b/r (fixed), h/b (fixed or free) and shrub radius (fixed or free); this was effected to constrain the results to physically possible or reasonable ranges by multiplying the mean-square error with a large number. The starting position was defined with all parameters except b/r ($=1.0$) set to typical values ($\lambda = 0.1656$, LAI $= 0.06$; shrub radius $= 0.25$ and $h/b = 1.5$, derived from PROVE and JORNEX measurements; see Asner et al., 2000, Ni & Li, 2000; Qin & Gerstl, 2000; White et al., 2000). The implication of allowing only two adjustable parameters—number density and LAI—is that the scene is modeled as if it consisted of a varying number density of plant protrusions all of the same height and shape and with a varying foliage density.

2.6. Validation protocol for retrieved SGM parameters

Panchromatic IKONOS images with a mapped GIFOV of 1 m were used to estimate protrusion (shrub and forb) density and planimetric cover; and multispectral IKONOS images with a mapped GIFOV of 4 m were used to estimate green leaf abundance (effective LAI) using NDVI for the grass site and the modified soil-adjusted vegetation index (MSAVI_2) for the transition site (the MSAVI_2 is arguably better adapted to situations where exposed soil is important; Qi, Chehbouni, Huete, Kerr, & Sorooshian, 1994). The broad variations in protrusion density, LAI, shrub width, and planimetric cover are obvious in very high resolution images although canopy height may only be estimated on the basis of knowledge of the species present (e.g. acacia groves) and through mesquite shrub size.

Table 2
Retrieved parameters and inversion statistics

	Inversion	LAI	#Density	Width (m)	h/b	Height (m)	Cover (%)	RMSE	R^2
(a) Transition site inversions									
Minimum	FD	0.00	0.51	*0.50*	*1.50*	§	9.5	0.01	0.93
	FDW	0.00	0.05	0.73	*1.50*	0.55	9.5	0.01	0.93
Maximum	FD	11.36	1.36	*0.50*	*1.50*	§	23.4	0.02	1.00
	FDW	11.32	0.34	2.26	*1.50*	1.69	23.4	0.02	1.00
Mean	FD	0.67	0.89	*0.50*	*1.50*	§	15.9	0.01	0.97
	FDW	0.80	0.21	1.08	*1.50*	0.81	15.9	0.01	0.97
Mode	FD	0.00	0.76	*0.50*	*1.50*	§	16.2	0.01	0.97
	FDW	0.00	0.08	0.75	*1.50*	0.56	15.1	0.01	0.98
Standard deviation	FD	1.70	0.18	§	§	§	2.9	0.00	0.01
	FDW	2.01	0.07	0.28	*1.50*	0.21	2.9	0.00	0.01
Coeffient of variation	FD	2.51	0.20	§	§	§	0.2	0.09	0.01
	FDW	2.53	0.35	0.26	§	0.26	0.2	0.09	0.01
(b) Grass site inversions									
Minimum	FD	0.00	0.67	*0.50*	*1.50*	§	12.3	0.01	0.78
	FDW	0.00	0.07	0.75	*1.50*	0.56	12.3	0.01	0.78
Maximum	FD	11.18	1.73	*0.50*	*1.50*	§	28.8	0.05	1.00
	FDW	11.91	0.43	1.94	*1.50*	1.45	28.8	0.05	1.00
Mean	FD	1.45	1.29	*0.50*	*1.50*	§	22.4	0.03	0.94
	FDW	1.49	0.30	1.07	*1.50*	0.80	22.3	0.03	0.94
Mode	FD	0.00	1.37	*0.50*	*1.50*	§	23.6	0.03	0.94
	FDW	0.00	0.33	1.00	*1.50*	0.75	23.5	0.03	0.94
Standard deviation	FD	3.15	0.17	§	§	§	2.7	0.01	0.02
	FDW	3.13	0.08	0.16	*1.50*	0.12	2.7	0.01	0.02
Coefficient of variation	FD	2.18	0.13	§	§	§	0.1	0.21	0.03
	FDW	2.10	0.26	0.15	§	0.15	0.1	0.21	0.03

§ = h/b, b and width were fixed (value irrelevant). F = LAI, D=#density, W = width. Italics indicate fixed values. Starting point: LAI = 0.06, #density = 0.1656, width = 0.5, $h/b = 0.1.5$.

3. Results and discussion

3.1. SGM validation results

In forward mode and for sun zeniths of 0°, 30° and 60° and viewing zeniths in the range ± 70°, the SGM produces bowl-shaped BRDF patterns in the principal plane and away from the hot spot, behaving as expected for values of shrub width, density and LAI in the ranges 0.05–2.00, 0.005–0.366, and 0.01–2.01, respectively (i.e. covering a wide range of likely configurations; Chopping, Su, Rango, & Maxwell, 2002). When parameterized by mean plant density, radius and *b*/*r* ratio, the SGM yields PP values and shapes which are very similar to those given by the explicit 3-D

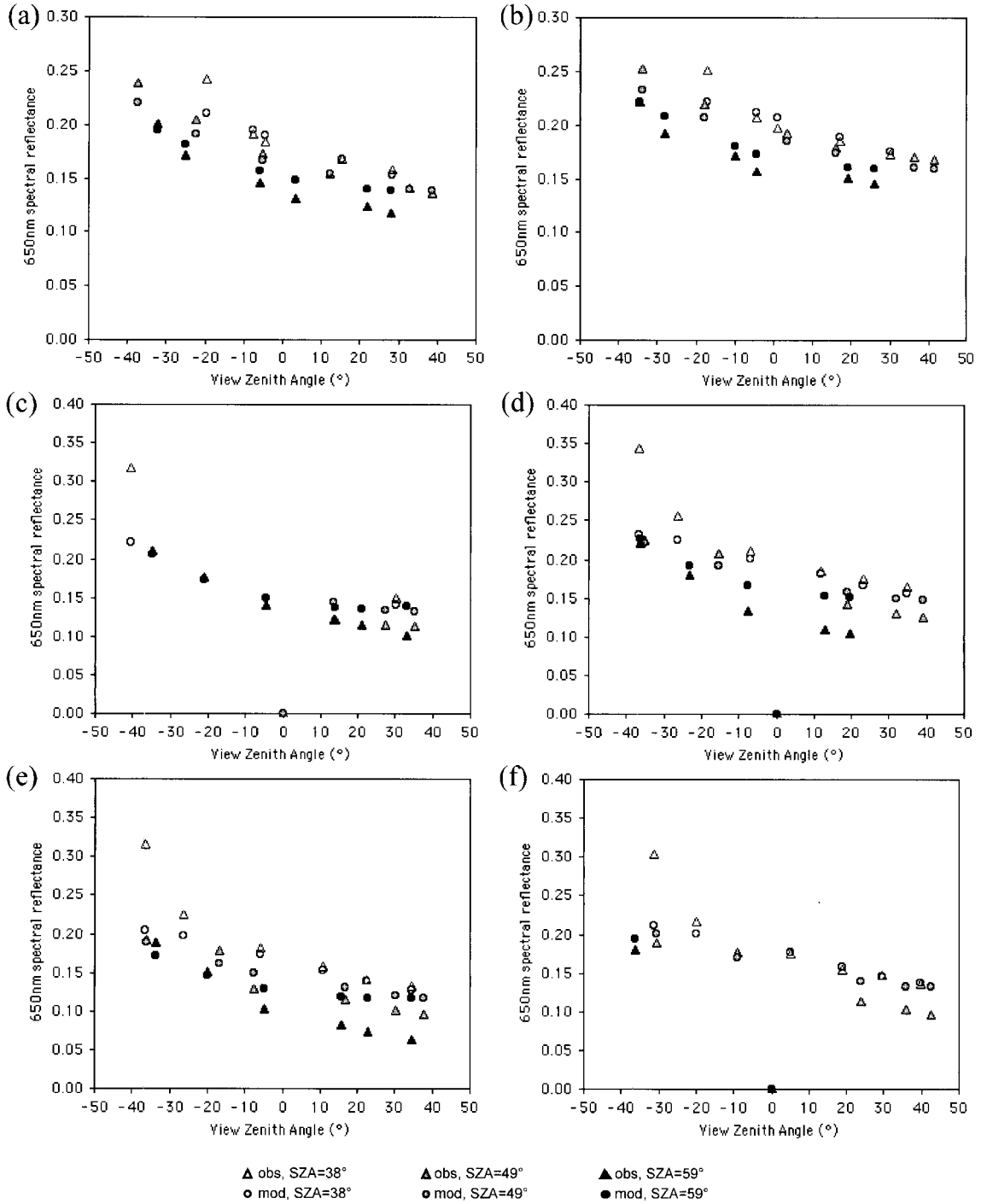

Fig. 7. Observed (obs) and modeled (mod) 650-nm bidirectional reflectance at three solar zenith angles for samples over the grass–shrub transition site (a–b) locations near the center of the target area with all 17 observations, (c) low density patch, (d) over the crossroads (e) over a dark background (probably annuals) and (f) a large mesquite shrub or acacia tree. Data points at zero on the *Y*-axis indicate missing data.

radiosity modeling effected with the RGM (Fig. 5). The SGM outputs for the two plots (sparse and dense understories) diverged from the multiangular observations and RGM outputs for the sparse plot with RMSE of 0.02 and 0.01 and R^2 of 0.91 and 0.98, respectively, and from the dense plot with RMSE of 0.04 and 0.02 and R^2 of 0.93 and 0.98, respectively. Divergence between the modeled outputs is small but is somewhat greater (< 6%) between the modeled outputs and the observations. This is probably a result of neglecting remnant (largely senescent) grass and its associated shadowing effects, since the deviation is greater in the dense plot and in the forward scattering direction at the higher 59° solar zenith angle (Table 1, Chopping, Su et al., 2002). A more comprehensive test of the match between the RGM output

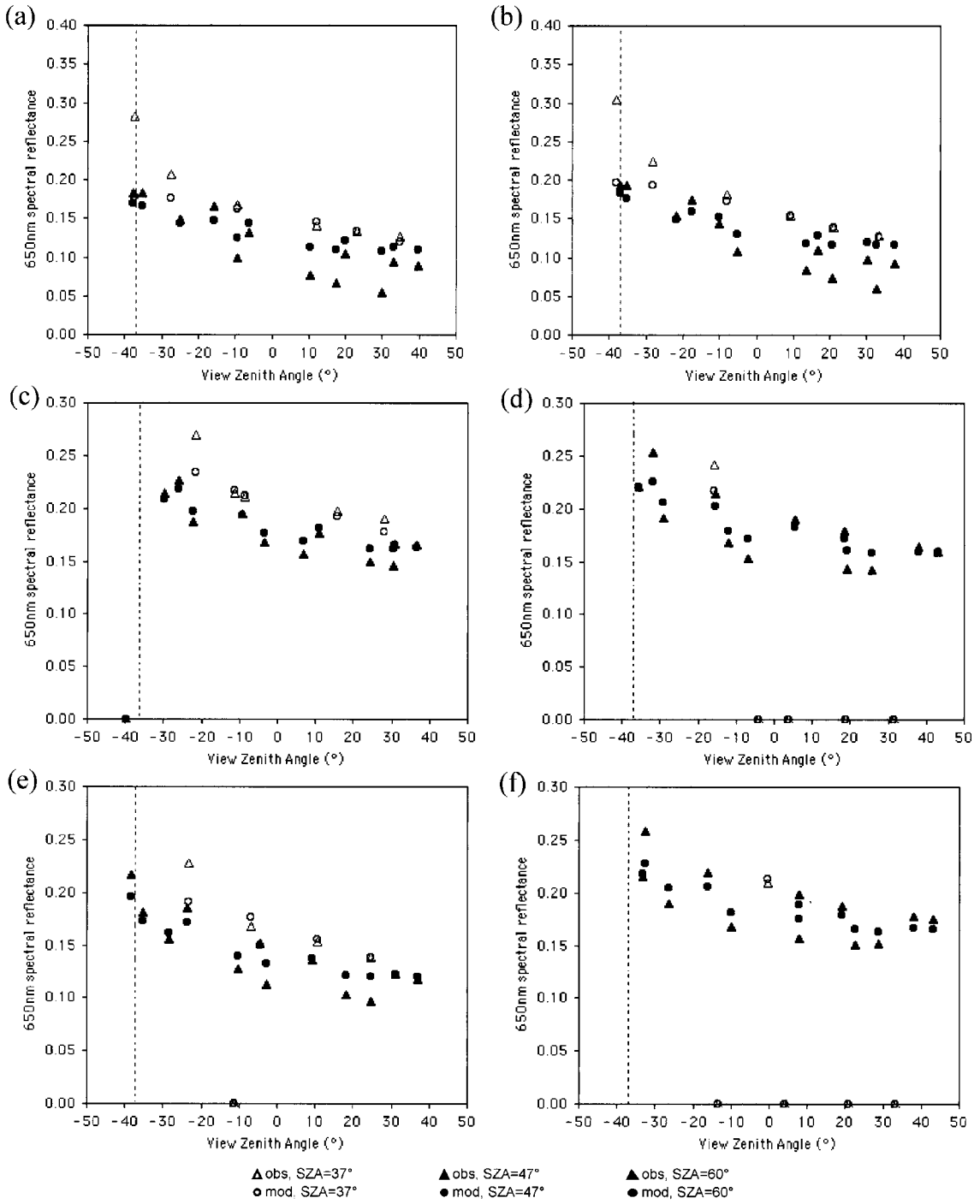

Fig. 8. Observed (obs) and modeled (mod) 650-nm bidirectional reflectance at three solar zenith angles for samples over the grass site (a)–(b) locations from the center of the target area with all 18 observations, (c) acacia/bare, (d) road, (e) medium cover grass, (f) sparse cover. The dotted line at VZA = 37° indicates the hot spot. Data points at zero on the *Y*-axis indicate missing data.

and the SGM—for the set of angular configurations defined by increments in relative azimuth angle of 30° and viewing zenith angle of 15° and at three sun zenith angles, $n = 186$—also demonstrated excellent matches, with R^2 of 0.90 and 0.91 for the sparse and dense plots, respectively (Fig. 6), and 0.92 and 0.91, respectively, if samples within 5° of the hot spot and specular directions are excluded.

3.2. SGM fits to observations

The model fits to observations over the transition site with inversion for two or three parameters are rather good, with all RMSE values <0.02 and all R^2 values >0.93 (Table 2(a); Fig. 7). The SGM had greater difficulty reproducing observed values at the 59° solar zenith angle, especially from nadir and into the forward-scattering direction. There is little difference in model fitting between inversions effected for two (LAI and density) and three parameters (LAI, density and width). The model fits to the grass site observations with simultaneous inversion for two or three parameters are also rather good, with all RMSE values ≤ 0.05 and all R^2 values >0.78 (Table 2(b); Fig. 8). The largest errors (differences between observed and modeled values) are consistently obtained closer to the hot spot geometry of VZA = SZA = 37° indicated by a dotted line in the figure. The discrepancy between observed and modeled reflectance in this region is almost an order of magnitude greater than that elsewhere but this is not surprising as the SGM has no mechanism for accounting for this phenomenon. With the exception of the hot spot, the SGM had greater difficulty reproducing observed values at the 59° solar zenith angle, especially from nadir and into the forward-scattering direction. This may be related to specular effects or to the greater difficulty of estimating spectral irradiance at high solar zenith angles, as the downwelling atmospheric path length is much greater. Again there is little difference in model fitting between the inversions effected for two parameters (LAI and density) and those effected for three parameters (LAI, density and width).

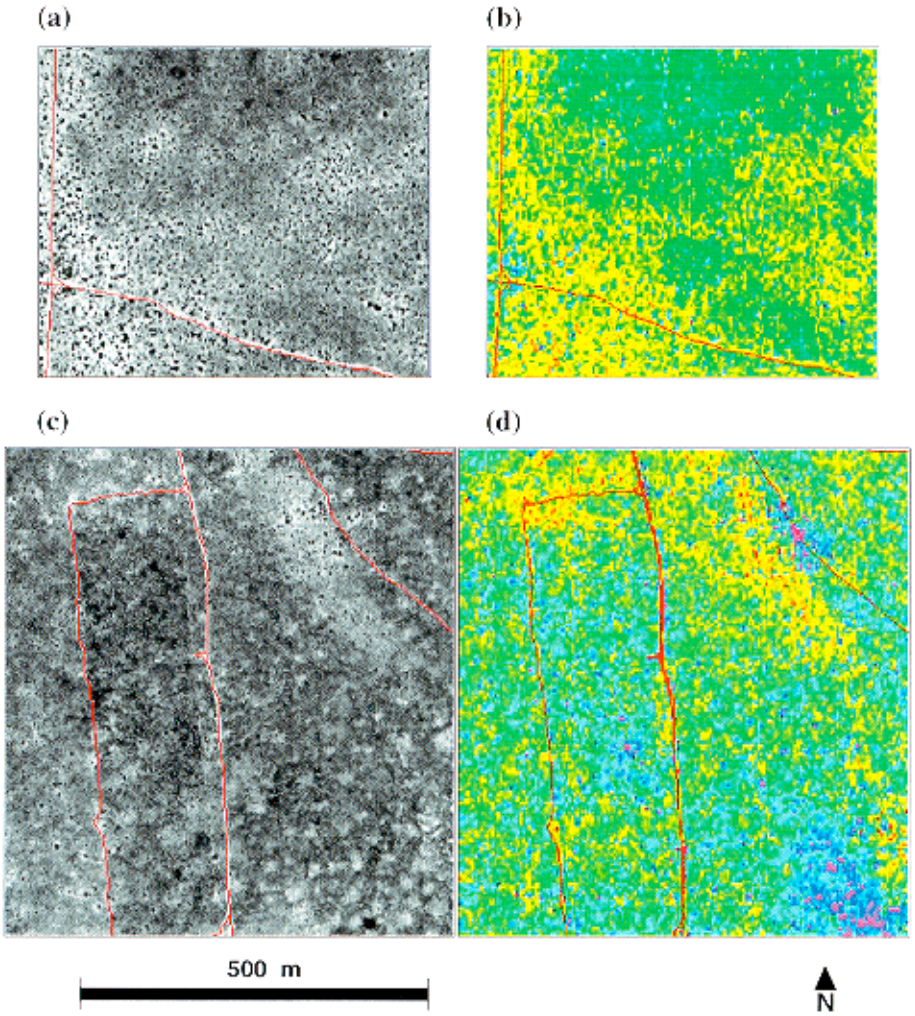

Fig. 9. Reference images: (a) transition site 1-m panchromatic IKONOS image, (b) transition site 4-m $MSAVI_2$ IKONOS image, (c) grass site 1-m panchromatic IKONOS image, (d) grass site 4-m NDVI IKONOS image. VI images are shown via a ROYGBIV LUT (red low; violet high). Red lines indicate roads and fencelines.

Note that it is not difficult to obtain good fits between a model and observations if the model parameters do not have a physical meaning or if the model is not sensitive to changes in parameter values. Sensitivity tests carried out on the SGM by varying one parameter at a time over the ranges of values typically encountered show that it is very sensitive to the input parameters and large changes are seen in the reflectance outputs (Chopping, Su et al., 2002); the results are therefore not spurious.

3.3. Value distributions of retrieved canopy attributes

Absolute values of retrieved parameters from the inversions for the transition site are mostly reasonable (Table 2(a)); mean LAI values for the two (three) parameter inversions was 0.67 (0.80), which compares well with LAI from ground measurements (0.59; Chopping, 2000). Mean number density differed somewhat at 0.89 (0.21), while all statistics for the fractional cover maps were similar with mimina, mean and maxima of 9.5%, 15.9% and 23.4%, respectively, comparing well with the range of 10%–20% obtained by aerial photography and profiling LIDAR measurements (Asner et al., 2000; White et al., 2000). Retrieved protrusion (shrub and forb) width values were in the range 0.73–2.26 m, which seems reasonable for creosote and mesquite shrubs at this site. For the grass site, mean LAI values were 1.45 (1.49), which is much greater than the ≈ 0.80 for both litter and green leaf given in Asner et al. (2000); however, the mode indicates that the distribution is importantly skewed, with most values in the range 0.0–1.44 (Table 2(b)). Moreover, this is for the peak of the growing season and includes scattering by yucca plants, which are by no means insignificant in this desert grassland landscape. Grass site protrusion number density ranges from 0.67 to 1.73 (0.07–0.43) with a mean of 1.29 (0.3); again this parameter varied importantly between inversions. Fractional cover values were again similar for both two- and three-parameter inversions at between 12.3% and 28.8%, with rather normal distributions and modes of 24% (current estimates are 35%–55%; Asner et al., 2000).

3.4. Spatial distributions of retrieved canopy attributes

One meter panchromatic and 4-m spectral vegetation indices from the IKONOS satellite were used to estimate spatial distributions of protrusion density and green foliage abundance and cover, respectively (Fig. 9). Two standard deviation stretches are applied to all parameter images but note that where LAI value distributions include a small number of outliers (usually in the region of 11.0–12.0), the range was set to 0.0–1.0 and the stretch was reapplied. The spatial distributions of retrieved LAI and protrusion density (two-parameter inversions) for the transition site are shown in Fig. 10(a) and (b). There were no observations

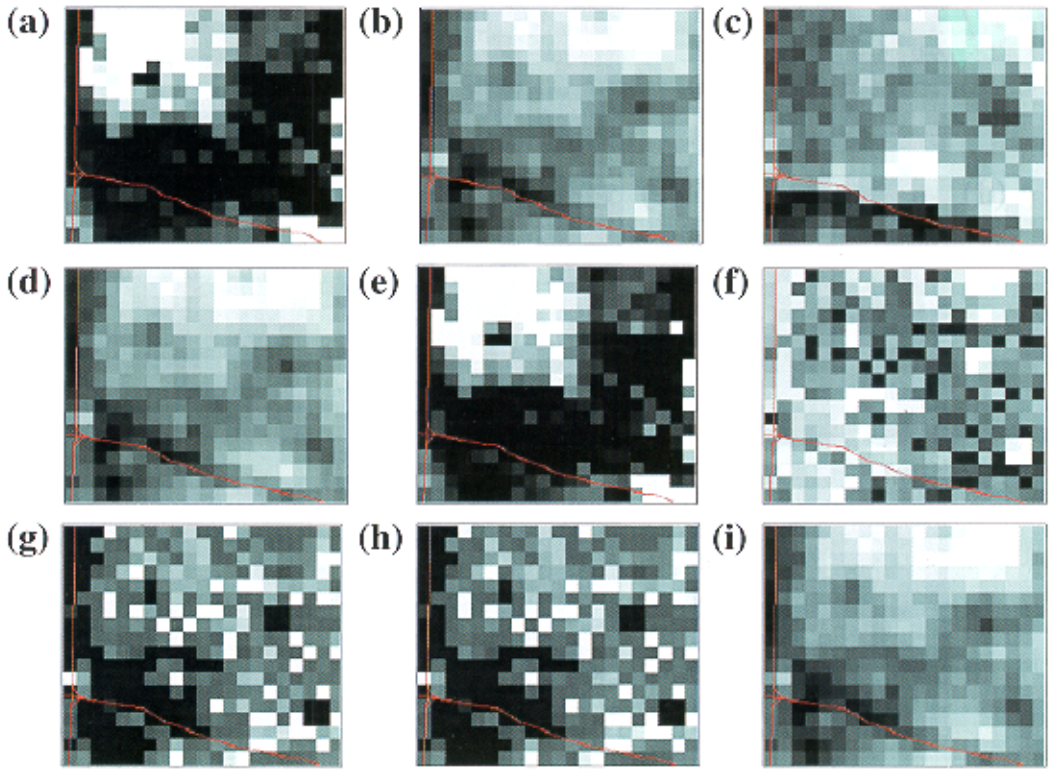

Fig. 10. Parameter maps (25-m cells) for the transition site from inversion of the SGM for density and LAI: (a) LAI, rescaled 0.0–1.0, (b) shrub density, (c) RMSE, (d) fractional cover; inversion of the SGM for density, LAI and width: (e) LAI, rescaled 0.0–1.0, (f) shrub density, (g) shrub width, (h) canopy height, (i) fractional cover. Red lines indicate roads. See Table 2 for inversion statistics.

close to the hot spot geometry over this site. The spatial distribution of retrieved LAI values is not closely related to vegetation vigor as indicated in the $MSAVI_2$ image, although note that the vegetation index is a composite measure of (horizontal) vegetation cover, (vertical) foliage density and leaf greenness, while the LAI map represents the absolute density of scatterers within each 25-m^2 area. The $MSAVI_2$ image was derived from multispectral IKONOS imagery (Fig.9(b)) and values follow the proportion of exposed ground; it shows little important variation across the target area with the notable exception of isolated mesquite and acacia plants and a bright, high-$MSAVI_2$ zone surrounding the crossroads. This latter feature is due to the greater sensitivity of the vegetation index to the presence of a small acacia grove, to leaf area as well as greenness, and to the greater proportion of annuals at this location, which is subject to greater disturbance by vehicles. The protrusion density map shows a lower value close to the crossroads and along the road in the SW quadrant and NW-most area, and higher values in the northern part of the target area, possibly related to occurrences of the annual snakeweed. The low number density patches in the center of the NW quadrant and in the center-right of the target area are related to patches where there is a small number of large plants such as acacia trees and large mesquite shrubs (appearing as large black dots in the 1-m panchromatic imagery; Fig. 9(a). The fractional cover map (Fig. 10(d)) derived from the retrieved parameters has a similar distribution to the protrusion density map. The RMSE map shows an area of higher deviation between the SGM and observations near the center of the target area and lower values in the southern part. The three-parameter inversions for the transition site yielded an LAI map (Fig. 10(e)) with a similar distribution to the two-parameter inversions but the distributions of protrusion density, width and canopy height are rather noisy (Fig. 10(f)–(h)): there is little obvious correlation between these and the high resolution reference images. The fractional cover map (Fig. 10(i)) retains the distribution obtained previously.

The spatial distributions of retrieved LAI and protrusion density parameters for the grass site (two-parameter inversions) are shown in Fig. 11(a) and (b), respectively. As with the transition site inversions of this kind, the LAI map does not appear to be in close agreement with the reference images. Again, higher values (in the NE quadrant) correspond to a cluster of acacia trees over rather bare soil towards

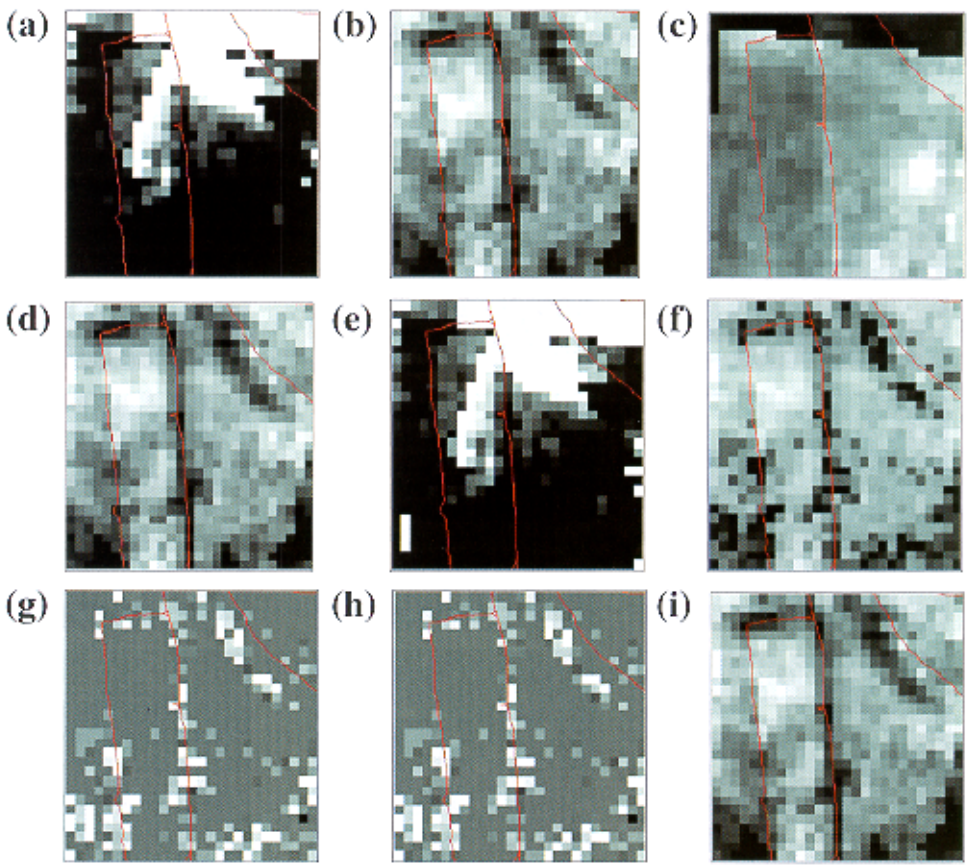

Fig. 11. Parameter maps (25-m cells) for the grass site from inversion of the SGM for density and LAI, with screening for observations within 5° of the hotspot: (a) LAI, rescaled 0.0–1.0, (b) shrub density, (c) RMSE, (d) fractional cover; from inversion of the SGM for density, LAI and width, with screening for observations within 5° of the hotspot: (e) LAI, rescaled 0.0–1.0, (f) shrub density, (g) shrub width, (h) canopy height, (i) fractional cover. Red lines indicate roads, paths and fencelines. See Table 2 for inversion statistics.

the bottom of a gentle slope to the NE, and elsewhere in this quadrant. The discrepancy between the LAI and index images may again be a result of the measurement of different phenomena. Protrusion density seems to follow foliage density as reflected in the NDVI reference image (Fig. 9(d)), rather than the density of yucca plants, although this is difficult to establish even from 1-m imagery. The RMSE map (Fig. 11(c)) shows larger deviations between the SGM and observations close to the location of the hot spot, as noted previously. The fractional cover map (Fig. 11(d)) has a spatial distribution similar to that of the density map.

The spatial distributions of retrieved LAI, protrusion density and shrub width parameters for the grass site (three-parameter inversions) are shown in Fig. 11(e) and (f), respectively. The LAI map is again in disagreement with the reference images, with a similar distribution to that obtained on inverting for two parameters. Protrusion density follows foliage density as reflected in the 4-m NDVI reference image (Fig. 9(d)) and is the inverse of the shrub width and canopy height distributions. This is reasonable since larger plants requisition greater water and soil resources, leading to lower numbers of plants per unit area. The shrub width and canopy height maps (Fig. 11(g) and (h)) have almost identical distributions, with bigger, taller plants distributed along the unmade road and fencelines and at the location of the acacia grove. These distributions correspond closely to the locations of larger plants, mainly mesquite shrubs and acacia; most of these can be seen clearly on the 1-m panchromatic reference image. The acacia trees have also been noted in field observations and outside these areas, plant width and canopy height are more uniform. The fractional cover map (Fig. 11 (i)) has a spatial distribution similar to that of the density map and appears as the inverse of the 1-m panchromatic reference image.

4. Conclusions

These results show that when adjusted against limited multiangular reflectance data, the SGM is able to provide information on canopy structure which is not available directly via nadir spectral approaches. Maps of fractional cover are related to cover estimated from high resolution imagery and absolute values are in the range given in the previous studies (Asner et al., 2000; White et al., 2000). The retrieved protrusion density, width and canopy height maps reveal variations in canopy physiognomy, distinguishing areas with large plants such as acacia and honey mesquite over sparse backgrounds from those with more uniform plant sizes. Protrusion density is the parameter which is retrieved most consistently, corroborating the results of Abuelgasim, Gopal, and Strahler (1998) who found that this was the most reliably estimated (of density, crown shape and canopy height) using a GO model for simulated forest, savanna and shrub landscapes. The maps of retrieved LAI values do not always appear to reflect the spatial distribution of all green vegetation at the end of the growing season, although this may be because the available IKONOS reference imagery was acquired some 2 months earlier (07/20/00) and patterns of green leaf abundance may change rapidly through the growing season as annuals take advantage of the moisture provided by large summer convective rainfall events. A further possible explanation is the very low LAI of the communities of these desert landscapes. The LAI maps do reflect the locations of larger shrubs and acacia trees rather consistently, with higher values where these features occur even when cover is low; i.e. plants are surrounded by very sparse lower vegetation. The angular sampling régime adopted was a minimal one and did not include observations away from the principal plane, although the data were acquired at a wide range of solar zenith angles. Future studies will be able to exploit data from the Multiangle Imaging SpectroRadiometer (MISR) sensor on NASA's Terra satellite and the CHRIS sensor (Sira Electro-Optics, UK) on the PROBA satellite. These will provide a better appreciation of the potential and limitations of multiangle remote sensing as a unique data source for acquiring information on the physical properties of desert soil–canopy complexes.

Acknowledgements

The authors gratefully acknowledge the assistance of the staff of the USDA, ARS Jornada Experimental Range, and in particular Eddie Garcia, Jim Lenz, Dave Thatcher and Rob Dunlap; researchers from the University of Arizona and in particular, Alfredo Huete, Karim Batchily and Gao Xiang; Betty Walter-Shea at the School of Natural Resource Sciences at the University of Nebraska-Lincoln; and Rob Parry at the Hydrology and Remote Sensing Laboratory, Beltsville, MD.

References

Abuelgasim, A. A., Gopal, S., & Strahler, A. H. (1998). Forward and inverse modelling of canopy directional reflectance using a neural network. *International Journal of Remote Sensing*, *19*(3), 453–471.

Asner, G. P., Wessman, C. A., Bateson, C. A., & Privette, J. L. (2000). Impact of tissue, canopy and landscape factors on reflectance variability of arid ecosystems. *Remote Sensing of Environment*, *74*, 69–84.

Barnsley, M. J., Allison, D., & Lewis, P. (1997). On the information content of multiple view angle (MVA) images. *International Journal of Remote Sensing*, *18*(9), 1937–1960.

BNSC (British National Space Centre) (2002). *New Low Cost UK Earth Observation Instrument Orbits the Earth on a European Satellite,* URL (last access 11/20/02): = http://www.bnsc.gov.uk/index.cfm?fast = news&action = readArticle&article = 35.

Brown de Colstoun, E. C., Vermote, E. R., Walthall, C. L., Cialella, A. T., Halthore, R. N., & Irons, J. R. (1996). Variability of BRDF with land cover type for the West Central HAPEX-Sahel Super Site. *Proc. IGARSS 1996, Lincoln, Nebraska* (pp. 1904–1907). Piscataway: IEEE.

Chen, J. M., Li, X., Nilson, T., & Strahler, A. (2000). Recent advances in geometrical optical modelling and its applications. *Special edition of Remote Sensing Reviews*, *18*(2–4), 227–262.

Chopping, M. J. (2000). Large-scale BRDF retrieval over New Mexico with a multiangular NOAA AVHRR dataset. *Remote Sensing of Environment, 74*(1), 163–191.

Chopping, M. J., Rango, A., & Ritchie, J. C. (2002). Improved semi-arid community type differentiation with the NOAA AVHRR via exploitation of the directional signal. *IEEE Transactions on Geoscience and Remote Sensing, 40*(5), 1132–1149.

Chopping, M. J., Su, L., Rango, A., & Maxwell, C. (2002). Modeling the reflectance anisotropy of Chihuahuan Desert grass–shrub transition canopy–soil complexes, submitted for publication.

Disney, M. I. (2002). *Improved estimation of surface biosphysical parameters through inversion of linear BRDF models*, unpublished PhD thesis, University College London.

Duncan, J., Stow, D., Franklin, J., & Hope, A. (1993). Assessing the relationship between spectral vegetation indices and shrub cover in the Jornada Basin, New Mexico. *International Journal of Remote Sensing, 14*(18), 3395–3416.

Everitt, J. H., Alaniz, M. A., Davis, M. R., Escobar, D. E., Havstad, K. M., & Ritchie, J. C. (1997). Light reflectance characteristics and video remote sensing of two range sites on the Jornada Experimental Range. *Proceedings of the 16th Biennial Workshop on Videography and Color Photography in Resource Assessment* (pp. 485–495). Bethesda, MD: American Society for Photogrametry and Remote Sensing.

Flasse, S. P. (1993). *Extracting Quantitative Information from Satellite Data: Empirical and Physical Approaches*, Institute for Remote Sensing Applications, Joint Research Centre, European Commission (EUR 15409EN), PhD dissertation, Faculté des Sciences Agronomiques at the Université Catholique de Louvain, Louvain-la-Neuve, Belgium.

Franklin, J., Duncan, J., & Turner, D. L. (1993). Reflectance of vegetation and soil in Chihuahuan desert plant communities from ground radiometry using SPOT wavebands. *Remote Sensing of Environment, 46*, 291–304.

Franklin, J., & Turner, D. L. (1992). The application of a geometric optical canopy reflectance model to semiarid shrub vegetation. *IEEE Transactions on Geoscience and Remote Sensing, 30*(2), 293–301.

Gemmell, F. (2000). Testing the utility of multi-angle spectral data for reducing the effects of background spectral variations in forest reflectance model inversion. *Remote Sensing of Environment, 72*, 46–63.

Havstad, K. M., Kustas, W. P., Rango, A., Ritchie, J. C., & Schmugge, T. J. (2000). Jornada Experimental Range: a unique arid land location for experiments to validate satellite systems. *Remote Sensing of Environment, 74*, 13–25.

Hlavka, C. A. (1986). *Simulation of Landsat MSS spatial resolution with airborne scanner data*, NASA Technical Memorandum 86832, 11 pp.

Hooke, R., & Jeeves, T. A. (1961, April). Direct search solution of numerical and statistical problems. *Journal of the Association for Computing Machinery, 8*, 212–229.

Huenneke, L. F., Anderson, J., Schlesinger, W. H., & Remmenga, M. (2001). *Plant biomass and aboveground net primary production in Chihuahuan Desert ecosystems: a ten-year record*, in review.

Jupp, D. L. B., McDonald, E. R., Harrison, B. A., Li, X., Strahler, A. H., & Woodcock, C. E. (1994). Prospects for mapping canopy structure using geometric-optical models. *Proceedings of the 7th Australasian Remote Sensing Conference, Melbourne, Australia, March 1–4*.

Kuusk, A., & Nilson, T. (2000). A directional multispectral forest reflectance model. *Remote Sensing of Environment, 72*, 244–252.

Leroy, M., Bicheron, P., & Hautecoeur, O. (1997). Extraction de paramètres biophysiques du couvert végétal à partir de capteurs satéllitaires à grand champs d'observation. In G. Guyot, & T. Phulpin (Eds.), *Physical Measurements and Signatures in Remote Sensing*. Proceedings of the ISPRS Conference, Courcheval, France, 7th–11th April, 1997 (pp. 391–400). Rotterdam: AA Balkema.

Li, X., Strahler, A. H., & Woodcock, C. E. (1995). A hybrid geometric optical-radiative transfer approach for modeling albedo and directional reflectance of discontinuous canopies. *IEEE Transactions on Geoscience and Remote Sensing, 33*(2), 466–480.

Moran, M. S., Bryant, R. B., Clarke, T. R., & Qi, J. (2001). Deployment and calibration of reference reflectance tarps for use with airborne imaging sensors. *Photogrammetric Engineering and Remote Sensing, 67*(3), 273–286.

Ni, W., & Li, X. (2000). A coupled vegetation–soil bidirectional reflectance model for a semi-arid landscape. *Remote Sensing of Environment, 74*(1), 113–124.

Pelgrum, H., Schmugge, T., Rango, A., Ritchie, J., & Kustas, W. (2000). Length scale analysis of surface albedo, temperature and NDVI in a desert grassland. *Water Resources Research, 36*(7), 1757–1765.

Pinty, B., Widlowski, J.-L., Gobron, N., Verstraete, M. M., & Diner, D. J. (2002, July). Uniqueness of multiangular measurements: Part 1. An indicator of subpixel surface heterogeneity from MISR. *IEEE Transactions on Geoscience and Remote Sensing, vol. 40, No. 7* (pp. 1560–1573).

Privette, P., Asner, G. P., Conel, J., Huemmrich, K. F., Olson, R., Rango, A., Rahman, A. F., Thome, K., & Walter-Shea, E. A. (2000). The EOS Prototype Validation Exercise (PROVE) at Jornada: overview and lessons learned. *Remote Sensing of Environment, 74*(1), 1–12.

Qi, J., Chehbouni, A., Huete, A. R., Kerr, Y. H., & Sorooshian, S. (1994). A modified soil adjusted vegetation index. *Remote Sensing of Environment, 48*, 119–126.

Qi, J., Huete, A. R., Cabot, F., & Chehbouni, A. (1994). Bidirectional properties and utilizations of high-resolution spectra from a semiarid watershed. *Water Resources Research, 30*(5), 1271–1279.

Qin, W., & Gerstl, S. A. W. (2000). 3-D scene modeling of Jornada semi-desert vegetation cover and its radiation regime. *Remote Sensing of Environment, 74*(1), 145–162.

Rango, A., Ritchie, J. C., Kustas, W. P., Schmugge, T. J., Brubaker, K. L., Havstad, K. M., Prueger, J. H., & Humes, K. S. (1996). JORNEX: a remote sensing campaign to quantify rangeland vegetation change and plant community–atmospheric interactions. *Proceedings of Second International Conference on GEWEX, Washington, DC* (pp. 445–446). Washington, DC: GEWEX/Global Climatic Research Programme (World Meteorological Organization).

Ross, J. K. (1981). *The radiation regime and architecture of plant stands*. The Hague: Dr. W. Junk Publishers, 392 pp.

Roujean, J.-L., Leroy, M., & Deschamps, P.-Y. (1992). A bidirectional reflectance model of the Earth's surface for the correction of remote sensing data. *Journal of Geophysical Research, 97*(D18), 20455–20468.

Schiebe, F. R., Waits, D. A., Everitt, J. H., & Duncan, J. (2001). Evaluation of the SST crop reflectance imaging system. *Proceedings of the 18th Biennial Workshop on Color Photography and Videography in Resource Assessment, American Society for Photogrammetry and Remote Sensing, May 16–18 2001, Amherst, MA*.

Vermote, E., Tanre, D., Deuze, J. L., Herman, M., & Morcrette, J. J. (1997). Second Simulation of the Satellite Signal in the Solar Spectrum (6S): An overview. *IEEE Transactions on Geoscience and Remote Sensing, 35*(3), 675–686.

Walthall, C. L., Norman, J. M., Welles, J. M., Campbell, G., & Blad, B. L. (1985). Simple equation to approximate the bidirectional reflectance from vegetative canopies and bare surfaces. *Applied Optics, 24*(3), 383–387.

Wanner, W., Li, X., & Strahler, A. H. (1995). On the derivation of kernels for kernel-driven models of bidirectional reflectance. *Journal of Geophysical Research, 100*, 21077–21090.

White, M. A., Asner, G. P., Nemani, R. R., Privette, J. L., & Running, S. W. (2000). Measuring fractional cover and leaf area index in arid ecosystems—digital camera, radiation transmittance, and laser altimetry methods. *Remote Sensing of Environment, 74*(1), 45–57.